On the Stability of Subsonic Impinging Jets

Gabriele Camerlengo[1], Jörn Sesterhenn[2], Flavio Giannetti[3], Vincenzo Citro[3(✉)], and Paolo Luchini[3]

[1] Institut für Strömungsmechanik und Technische Akustik, Technische Universität Berlin, Müller-Breslau-Straße 15, 10623 Berlin, Germany
gabriele.camerlengo@tu-berlin.de
[2] Lehrstuhl für Technische Mechanik und Strömungsmechanik, Universität Bayreuth, Universitätsstraße 30, 95447 Bayreuth, Germany
[3] Dipartimento di Ingegneria Industriale, Università degli Studi di Salerno, Via Giovanni Paolo II 132, 84084 Fisciano, SA, Italy
vcitro@unisa.it

Abstract. Impinging jets are relevant in many applications, especially those involving heating and cooling processes. In such context, several techniques have been proposed to enhance the heat transfer at the wall: in particular, experimental investigations demonstrated that the use of a pulsating inlet with an appropriate pulsation frequency may result in a 40% enhancement of heat transfer compared to a non-pulsating configuration. Such a result is related to the enlargement of the generated toroidal vortices which cause higher wall shear stresses. The mechanism underlying the generation of these larger vortex rings at a specific frequency is still unclear and the explanation of the effects of pulsation on heat transfer is still an open question. In order to shed light on such process, in this work, we present a modal analysis of a subsonic impinging jet confined between two horizontal walls placed at a distance of $5D$, being D the diameter of the orifice in the uppermost wall from which the jet issues. Initially, a direct numerical simulation (DNS) of a round jet with a Mach number of 0.8 and a Reynolds number of 3300 is performed and the main flow characteristics (including dominant frequencies and spatial features) are retrieved through a dynamic mode decomposition (DMD) analysis. Subsequently, a global stability analysis on the same physical configuration is carried out and the spatial structures and frequencies of the resulting leading unstable modes are discussed and compared with the DMD and DNS data.

Keywords: Compressible flows · Impinging jets · Direct numerical simulation · Dynamic mode decomposition · Stability analysis · Heat transfer

1 Introduction

Impinging jets are relevant in a considerable number of industrial and natural configurations. In particular, impinging jet systems are widely used in heating

A. Carcaterra et al. (Eds.): AIMETA 2019, LNME, pp. 99–116, 2020.
https://doi.org/10.1007/978-3-030-41057-5_8

and cooling processes because they may enhance the local heat transfer by more than an order of magnitude, compared to classical wall boundary layers [1].

In such context, the analysis of the jet geometry, the effects of the Reynolds and Mach numbers, and the shape of the impacted surface received great attention in the last decades. In industrial applications, typical flow configurations are confined in order to maximize the heat-transfer efficiency. Recent investigations proposed several techniques to increase this efficiency. In particular, it has been demonstrated that the use of a pulsating inlet with an appropriate pulsation frequency can result in a 40% enhancement of heat transfer compared to a non-pulsating configuration [2]. Such effect is related to the enlargement of the generated toroidal vortices which cause a higher shear stresses at the wall.

In order to better understand the physics of such phenomenon and determine the optimal forcing frequency it is fundamental to determine the modal characteristics of the unforced jet flow. For this purpose, different kind of techniques can be used: here we will make use of both modal linear stability analysis and DMD analysis to unveil the behavior and the fundamental frequencies of the jet.

Linear modal theory [3] has been successfully used to characterize the stability and transition to turbulence in a wide range of applications, both in the incompressible [4–9] and compressible [10] regimes. Meliga and Chomaz [9] investigated the planar impinging jet by using the linear stability theory. They proposed two different adjoint-based control strategies and discussed an open-loop control in which a small airfoil is introduced in the flow field. Yamouni et al. [10] performed a full compressible global stability analysis of a flow over an open cavity. Recently, Fani et al. [11] analyzed the sound generated by the flow around a circular cylinder with particular attention to the study of the acoustic emissions generated at low Mach and Reynolds numbers. The authors performed a global stability analysis by using the compressible linearized Navier-Stokes equations (see the review paper by Fabre et al. [12] for further details). The resulting leading modes provided detailed information related to the underlying hydrodynamic instability and data on the acoustic field generated. The DMD analysis is also adopted here to analyze the time-evolution of fluid flows. This technique was first introduced by Schmid and Sesterhenn [13] and has soon received a wide acceptance and interest from the fluid dynamics community.

Linear stability analysis and DMD can be regarded as two complementary approaches to perform a modal analysis of fluid dynamic system. The DMD attempts to decompose the fluid dynamic field into modes by using a series of time snapshots of flow. Furthermore, it can be carried out, in principle, at any Reynolds number, even when turbulence is fully developed. The necessary time-series of data must be obtained from experimental investigations or three-dimensional DNS computations. This is due to the fact that turbulence, with a few special exceptions, is a three-dimensional phenomenon. The computation of a DNS is generally expensive and its use is justified because it serves more purposes than only that of source for DMD data. On the other hand, a linear stability analysis can be often performed in a two-dimensional fashion when the third homogeneity direction does not play a role in the onset of the instabilities. This

reduces drastically the computational effort, if compared to a DNS of the same case. However, the application range of the linear stability analysis is limited by the transition to turbulence and by the fact it cannot take into account any nonlinear effect.

2 Theoretical Framework

2.1 Flow Configuration and Governing Equations

We investigate the round impinging jet flow delimited by two horizontal flat walls, as sketched in Fig. 1. The jet issues from an orifice of diameter D in the uppermost wall and impinges on the lowermost one (target plate). The distance between the walls is equal to $5D$, whereas their temperature is kept constant at 373.15 K, higher than the total temperature of the jet core at the inlet which is 293.15 K. The remaining boundaries are outlets. The considered Newtonian fluid is an ideal gas with a Prandtl number $Pr = 0.7$ and a heat capacity ratio $\gamma = 1.4$.

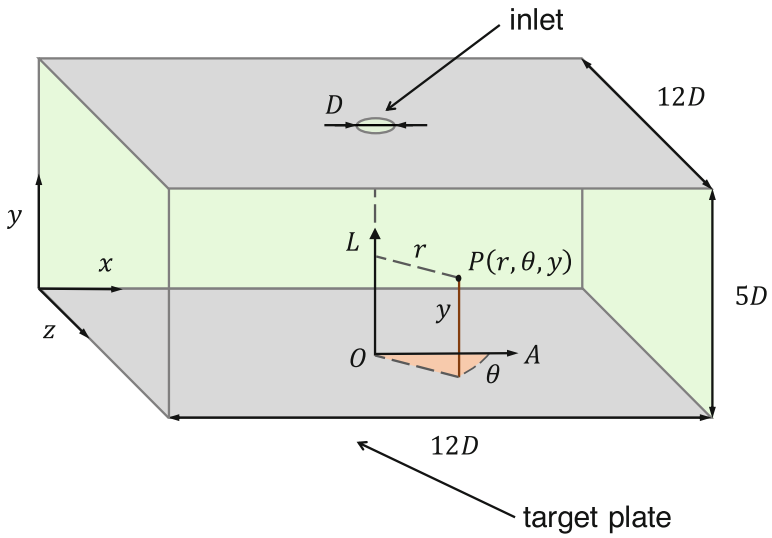

Fig. 1. Sketch of the computational domain, representing both the Cartesian and cylindrical reference systems adopted in this paper. Walls are colored in grey. D indicates the orifice diameter.

The flow dynamics is governed by the compressible Navier-Stokes equations[1]:

$$\frac{\partial \rho}{\partial t} + \boldsymbol{u} \cdot \nabla \rho + \rho \nabla \cdot \boldsymbol{u} = 0, \tag{1a}$$

$$\rho \frac{\partial \boldsymbol{u}}{\partial t} + \rho \boldsymbol{u} \cdot \nabla \boldsymbol{u} + \nabla p - \frac{1}{Re} \nabla \cdot \boldsymbol{\tau}(\boldsymbol{u}) = \boldsymbol{0}, \tag{1b}$$

$$\rho \frac{\partial T}{\partial t} + \rho \boldsymbol{u} \cdot \nabla T + (\gamma - 1)\, \rho T \nabla \cdot \boldsymbol{u} - \gamma\, (\gamma - 1)\, \frac{M^2}{Re} \boldsymbol{\tau}(\boldsymbol{u}) : \boldsymbol{S}(\boldsymbol{u}) - \frac{\gamma}{Pr\, Re} \nabla^2 T = 0, \tag{1c}$$

$$\rho T - 1 - \gamma M^2 p = 0, \tag{1d}$$

where $\boldsymbol{u}(\boldsymbol{x}, t)$ is the fluid velocity field, $p(\boldsymbol{x}, t)$ the pressure, $\rho(\boldsymbol{x}, t)$ the density, $T(\boldsymbol{x}, t)$ the temperature, $\boldsymbol{S}(\boldsymbol{u}) = \frac{1}{2}\left(\nabla \boldsymbol{u} + \nabla \boldsymbol{u}^{\mathrm{T}}\right)$ is the strain tensor and $\boldsymbol{\tau}(\boldsymbol{u}) = \left[2\boldsymbol{S}(\boldsymbol{u}) - \frac{2}{3}(\nabla \cdot \boldsymbol{u})\boldsymbol{I}\right]$ is the stress tensor per unit viscosity. System (1a–d) is made non-dimensional by using the incoming velocity U_∞ and the related reference density ρ_∞, temperature T_∞ and pressure p_∞, being the last field normalized as follows:

$$p = \frac{P - p_\infty}{p_\infty U_\infty^2} \tag{2}$$

with P the absolute dimensional pressure. The reference Reynolds and Mach numbers are respectively defined as

$$Re = \frac{\rho_\infty U_\infty D}{\mu}, \qquad M = \frac{U_\infty}{\sqrt{\gamma R T_\infty}} \tag{3}$$

where R is the specific ideal gas constant and μ the gas dynamic viscosity.

In order to mimic the (underdeveloped) flow issuing from a short nozzle, the inlet velocity and temperature profiles are assumed to be described by hyperbolic tangent functions, namely

$$u_2 = T = -\tanh \frac{D - 2r}{2D f_t} \Big/ \tanh \frac{1}{2 f_t}, \tag{4}$$

being u_2 the fluid velocity in y direction, r the distance from the jet axis (symmetry axis) and $f_t = 0.1$ a thickness parameter. The other components of the velocity as well as the pressure are set to 0. The relative non-dimensional pressure at the outlet surfaces is enforced to 0.

Taking advantage of the axial symmetry of the steady base flow, the stability and sensitivity analysis is performed in a cylindrical reference system. Only axially symmetric modes have been considered in this work, since it is well known from theoretical and experimental investigations [14] that for subsonic jets these are the dominant ones. Moreover, to avoid nonphysical reflections of acoustic waves at the edge of the computational domain, sponges have been implemented for both DNS and stability computations. Additional details are available in the studies by Fani et al. [11] and Wilke and Sesterhenn [15].

[1] Here, a non-conservative form of the Navier-Stokes equations is used because of their better conditioning and because of the absence of shocks in the flow.

2.2 Stability and Sensitivity Analysis

The stability analysis of the flow is based on the classical linear theory and normal-mode analysis. The solution $\boldsymbol{q}(\boldsymbol{x},t) = \{\boldsymbol{u}, p, T, \rho\}$ is expressed as the sum of a steady state field $\boldsymbol{q}_b(\boldsymbol{x}) = \{\boldsymbol{U}_b, P_b, T_b, \rho_b\}$, referred to as the base flow, and a small unsteady disturbance field $\boldsymbol{q}'(\boldsymbol{x},t) = \{\boldsymbol{u}', p', T', \rho'\}$, i.e.

$$\boldsymbol{q}(\boldsymbol{x},t) = \boldsymbol{q}_b(\boldsymbol{x}) + \boldsymbol{q}'(\boldsymbol{x},t). \tag{5}$$

In order to investigate the asymptotic stability of the flow, the evolution of the perturbation is decomposed into modes of normal form [16]

$$\boldsymbol{q}'(\boldsymbol{x},t) = \sum_i \hat{\boldsymbol{q}}_i(\boldsymbol{x}) \cdot \exp(\lambda_i t) + \text{c.c.} \tag{6}$$

with c.c. indicating the complex conjugate. According to Eq. (5), perturbations are described by the complex eigenmodes $\hat{\boldsymbol{q}}_i$ and the corresponding eigenvalues $\lambda_i = \sigma_i + i\omega_i$, where ω_i is the eigenfrequency and σ_i the growth rate. By substituting Eq. (5) into Eqs. (1a–d), we obtain two sets of equations, namely one for the underlying base flow, i.e.

$$\boldsymbol{U}_b \cdot \nabla\rho_b + \rho_b \nabla \cdot \boldsymbol{U}_b = 0, \tag{7a}$$

$$\rho_b \boldsymbol{U}_b \cdot \nabla \boldsymbol{U}_b + \nabla P_b - \frac{1}{Re}\nabla \cdot \boldsymbol{\tau}(\boldsymbol{U}_b) = \boldsymbol{0}, \tag{7b}$$

$$\begin{aligned}\rho_b \boldsymbol{U}_b \cdot \nabla T_b + (\gamma-1)\rho_b T_b \nabla \cdot \boldsymbol{U}_b - \gamma(\gamma-1)\frac{M^2}{Re}\boldsymbol{\tau}(\boldsymbol{U}_b) : \boldsymbol{S}(\boldsymbol{U}_b) \\ - \frac{\gamma}{Pr\,Re}\nabla^2 T_b = 0,\end{aligned} \tag{7c}$$

$$\rho_b T_b - 1 - \gamma M^2 P_b = 0, \tag{7d}$$

and a second one, a generalized eigenvalue problem, which provides eigenvalues and eigenmodes of the system, i.e.

$$\lambda_i \hat{\rho}_i + \boldsymbol{U}_b \cdot \nabla\hat{\rho}_i + \hat{\boldsymbol{u}}_i \cdot \nabla\rho_b + \rho_b \nabla \cdot \hat{\boldsymbol{u}}_i + \hat{\rho}_i \nabla \cdot \boldsymbol{U}_b = 0, \tag{8a}$$

$$\begin{aligned}\lambda_i \rho_b \hat{\boldsymbol{u}}_i + \hat{\rho}_i \boldsymbol{U}_b \cdot \nabla \boldsymbol{U}_b + \rho_b \hat{\boldsymbol{u}}_i \cdot \nabla \boldsymbol{U}_b + \rho_b \boldsymbol{U}_b \cdot \nabla \hat{\boldsymbol{u}}_i \\ + \nabla\hat{p}_i - \frac{1}{Re}\nabla \cdot \tau(\hat{\boldsymbol{u}}_i) = \boldsymbol{0},\end{aligned} \tag{8b}$$

$$\begin{aligned}&\rho_b \hat{T}_i \lambda_i + \hat{\rho}_i \boldsymbol{U}_b \cdot \nabla T_b + \rho_b \hat{\boldsymbol{u}}_i \cdot \nabla T_b + \rho_b \boldsymbol{U}_b \cdot \nabla \hat{T}_i \\ &+ (\gamma-1)\left(\hat{\rho}_i T_b \nabla \cdot \boldsymbol{U}_b + \rho_b \hat{T}_i \nabla \cdot \boldsymbol{U}_b + \rho_b T_b \nabla \cdot \hat{\boldsymbol{u}}_i\right) \\ &- \gamma(\gamma-1)\frac{M^2}{Re}\left[\tau(\hat{\boldsymbol{u}}_i) : \boldsymbol{S}(\boldsymbol{U}_b) + \tau(\boldsymbol{U}_b) : \boldsymbol{S}(\hat{\boldsymbol{u}}_i)\right] \\ &- \frac{\gamma}{Pr\,Re}\nabla^2 \hat{T}_i = 0,\end{aligned} \tag{8c}$$

$$\hat{\rho}_i T_b + \rho_b \hat{T}_i - \gamma M^2 \hat{P}_i = 0. \tag{8d}$$

The base flow problem (7a–d) is closed by the boundary conditions described in Sect. 2.1. The boundary conditions for the stability problem (8a–d) are derived

consistently. It is worth recalling, in conclusion, that a negative growth rate identifies a linearly stable mode, whereas a positive growth rate a linearly unstable mode.

2.3 Dynamic Mode Decomposition

In the present paper we use also the DMD analysis to unveil the behavior and the fundamental frequencies of the jet. Here, we briefly summarize the main concepts of this theory.

Given a system that evolves over time, the dynamic mode decomposition (DMD) allows the decomposition of its status into modes, each one associated with a frequency and a corresponding growth or decay rate. Thanks to this method, it is possible to approximate eigenvalues and eigenmodes of large systems whose transition matrices are unknown or hard to compute. In the following we outline the DMD method applied to flow field data as discussed by Schmid [17].

Let us consider a sequence of N snapshots of flow field data that are evenly spaced in time by an interval Δt,

$$\boldsymbol{Q}_1^N = \{\boldsymbol{q}_1, \boldsymbol{q}_2, \boldsymbol{q}_3, \ldots, \boldsymbol{q}_N\}. \tag{9}$$

We assume the existence of a linear operator $\boldsymbol{A}$ that maps the i-th flow field $\boldsymbol{q}_i$ to the successive flow field $\boldsymbol{q}_{i+1}$, namely,

$$\boldsymbol{q}_{i+1} = \boldsymbol{A}\boldsymbol{q}_i, \tag{10}$$

being $\boldsymbol{A}$ constant over the sampling interval $[0, (N-1)\,\Delta t]$. A sequence of flow fields can then be expressed as a Krylov sequence

$$\boldsymbol{Q}_1^N = \left\{\boldsymbol{q}_1, \boldsymbol{A}\boldsymbol{q}_1, \boldsymbol{A}^2\boldsymbol{q}_1, \ldots, \boldsymbol{A}^{N-1}\boldsymbol{q}_1\right\}. \tag{11}$$

With increasing time and thus N, it is assumed that the vectors in the sequence $\boldsymbol{Q}_1^N$ become linearly dependent. This means that with this approximation, if $N-1$ is the maximum number of linearly independent flow fields, the N-th field can be expressed as linear combination of the previous fields,

$$\boldsymbol{q}_N = a_1\boldsymbol{q}_1 + a_2\boldsymbol{q}_2 + \ldots + a_{N-1}\boldsymbol{q}_{N-1} + \boldsymbol{r} \tag{12}$$

or equivalently

$$\boldsymbol{q}_N = \boldsymbol{Q}_1^{N-1}\boldsymbol{a} + \boldsymbol{r} \tag{13}$$

where $\boldsymbol{a}^{\mathrm{T}} = \{a_1, a_2, \ldots, a_{N-1}\}$ and $\boldsymbol{r}$ the residual vector. By rewriting Eq. (9) for $N-1$ fields and left multiplying by $\boldsymbol{A}$, one obtains

$$\boldsymbol{A}\{\boldsymbol{q}_1, \boldsymbol{q}_2, \boldsymbol{q}_3, \ldots, \boldsymbol{q}_{N-1}\} = \{\boldsymbol{q}_2, \boldsymbol{q}_3, \boldsymbol{q}_4, \ldots, \boldsymbol{q}_N\} \tag{14}$$

which, by using Eq. (12), yields

$$\boldsymbol{A}\{\boldsymbol{q}_1, \boldsymbol{q}_2, \boldsymbol{q}_3, \ldots, \boldsymbol{q}_{N-1}\} = \boldsymbol{A}\left\{\boldsymbol{q}_2, \boldsymbol{q}_3, \boldsymbol{q}_4, \ldots, \boldsymbol{q}_{N-1}, \boldsymbol{Q}_1^{N-1}\boldsymbol{a}\right\} + \boldsymbol{r}\left(\boldsymbol{e}^{N-1}\right)^{\mathrm{T}} \tag{15}$$

or equivalently

$$\boldsymbol{A}\boldsymbol{Q}_1^{N-1} = \boldsymbol{Q}_2^N = \boldsymbol{Q}_1^{N-1}\boldsymbol{S} + \boldsymbol{r}\left(\boldsymbol{e}^{N-1}\right)^{\mathrm{T}} \tag{16}$$

with

$$e_i^N = \begin{cases} 1 & \text{if } i = N, \\ 0 & \text{otherwise,} \end{cases} \qquad i = 1, \ldots, N, \tag{17}$$

and $\boldsymbol{S}$ a companion matrix with size $(N-1) \times (N-1)$,

$$\boldsymbol{S} = \begin{pmatrix} 0 & & & a_1 \\ 1 & 0 & & a_2 \\ & \ddots & \ddots & \vdots \\ & & 1 & 0 \; a_{N-2} \\ & & & 1 \; a_{N-1} \end{pmatrix}. \tag{18}$$

The last column of $\boldsymbol{S}$ contains the unknown coefficients $\{a_1, a_2, \ldots, a_{N-1}\}$, which express the linear representations of the last field $\boldsymbol{q}_N$ in terms of the previous ones $\{\boldsymbol{q}_1, \boldsymbol{q}_2, \ldots, \boldsymbol{q}_{N-1}\}$. The eigenvalues of $\boldsymbol{S}$ approximate some of the eigenvalues of $\boldsymbol{A}$. The matrix $\boldsymbol{A}$ is in fact projected onto the subspace defined by $\boldsymbol{Q}_1^{N-1}$, similarly as in the Arnoldi method, where a matrix is projected onto successive Krylov subspaces.

Although the vector $\boldsymbol{a}$ can be computed by least square solution of the Eq. (13), a direct calculation of the modes based $\boldsymbol{S}$ is ill-conditioned and often does not produce good results. Therefore, it is common to transform $\boldsymbol{S}$ into a similar full matrix $\tilde{\boldsymbol{S}}$ by means of singular value decomposition of the field sequence $\boldsymbol{Q}_1^{N-1} = \boldsymbol{U}\boldsymbol{\Sigma}\boldsymbol{V}^{\mathrm{H}}$. By substituting $\boldsymbol{U}\boldsymbol{\Sigma}\boldsymbol{V}^{\mathrm{H}}$ into Eq. (16) and rearranging, one obtains

$$\boldsymbol{U}^{\mathrm{H}}\boldsymbol{A}\boldsymbol{U} = \boldsymbol{U}^{\mathrm{H}}\boldsymbol{Q}_2^N\boldsymbol{V}\boldsymbol{\Sigma}^{-1} \equiv \tilde{\boldsymbol{S}}. \tag{19}$$

Once the eigenvalues of $\tilde{\boldsymbol{S}}$ are calculated, the modal structures of the dynamic modes can be recovered by projecting its eigenvectors onto the basis $\boldsymbol{U}$, namely

$$\boldsymbol{\Phi}_i = \boldsymbol{U}\boldsymbol{v}_i \tag{20}$$

being $\boldsymbol{v}_i$ the i-th eigenvector of $\tilde{\boldsymbol{S}}$ and $\boldsymbol{\Phi}_i$ the associated i-th dynamic mode. It is worth recalling that the complex eigenvalues of $\tilde{\boldsymbol{S}}$, which provide an approximation of the eigenvalues of $\boldsymbol{A}$, can be written as $\lambda_i = \sigma_i + i\omega_i$, where ω_i represents the frequency of the i-th dynamic modes and σ_i its growth rates.

3 Numerical Setup and Validation

The jet problem has been tackled by using two different numerical approaches. First a full 3D DNS has been performed using an in-house highly-parallel finite-difference code [18] and a DMD analysis has been carried out on the generated DNS data set. Additionally, a stability analysis has been carried out using a finite-element method based on the software FreeFem++ (https://freefem.org).

Results from both approaches have been used together to analyze the physical characteristics of the problem and cross-validate the numerics: a very good agreement in terms of characteristics frequencies have been obtained, providing important information to unveil the nature of the self sustained instability.

3.1 Direct Numerical Simulation

Direct numerical simulation is achieved by using finite-difference methods for the spacial discretization. In particular, the 6th order compact central scheme by Lele [19] is applied to the diffusive term, whereas the 5th order upwind scheme by Adams and Shariff [20] is applied to the convective term. To advance in time, a classical low-storage 4th Runge-Kutta method is implemented. The computational domain is discretised on a rectilinear grid with 1024 points in each direction. The grid is refined near the lowermost wall in order to ensure a $y^+ < 0.6$ at every first node above the wall, being y^+ the dimensionless wall coordinate. A refinement around the jet axis is also applied, which causes the grid spacing in x and z directions to vary between $0.0099D$ and $0.0296D$, with D the jet diameter. For a validation of the grid in terms of Kolmogorov length scale, the reader may refer to Wilke and Sesterhenn [15] (case #6).

At the walls, isothermal non-slip boundary conditions are applied. Inflow conditions are enforced as discussed in Sect. 2.1. The lateral boundaries, which serve as outlets, implement acoustically non-reflecting boundary conditions [18]. To facilitate the outflow, a sponge region is also active for $r/D > 5$. The sponge acts as a forcing term in the Navier-Stokes equations that is proportional to the difference between the instantaneous field and some local reference values. These latter are imposed equal to the mean values in this domain region of a previous LES carried out on a wider domain extended in the x and y directions.

3.2 Stability and Sensitivity Analysis

A finite-element method has been used to perform the stability analysis addressed in this paper. The base flow $\boldsymbol{q}(\boldsymbol{x})$ and the perturbation eigenmodes $\hat{\boldsymbol{q}}_i(\boldsymbol{x})$ are described on an unstructured grid obtained through the Delaunay triangulation method. More specifically, the FreeFem++ built-in mesh generator (Bamg) has been used. The numerical problem has been discretized with the help of the FreeFem++ libraries by means of P2 elements for the velocity components and P1 elements for the pressure, temperature and density fields. The resulting nonlinear system of algebraic equations for the base flow has been solved by using a Newton-Raphson scheme. The linear operator arising from Eqs. (8a–d) has been inverted by means of the multifrontal, sparse LU solver MUMPS [21], whereas the library ARPACK has been used to solve the associated eigenvalue problem. The parametric tracking and computation of the leading direct and adjoint modes has been carried out with an inverse-iteration algorithm.

The computational domain is subdivided into two zones: a physical region and a sponge region. The first is defined as the region with $0 < r/D < 6$ and $0 < y/D < 5$, whereas the latter spans $6 < r/D < 50$ and $5 < y/D < 25$. Following

the approach by Rowley et al. [22], a forcing term in the form $-\beta(\boldsymbol{x})\,(\boldsymbol{q}-\boldsymbol{q}_r)$ has been added to the right-hand side of the governing equations in the sponge region, where $\beta(\boldsymbol{x})$ is an appropriate damping function and $\boldsymbol{q}_r(\boldsymbol{x})$ the reference field. Different meshes have been used: the largest one consists of approximately 700,000 triangles. The parametric studies have been performed on a grid with approximately 400,000 triangles and refined regions close to the wall and in the jet shear layer (Fig. 2).

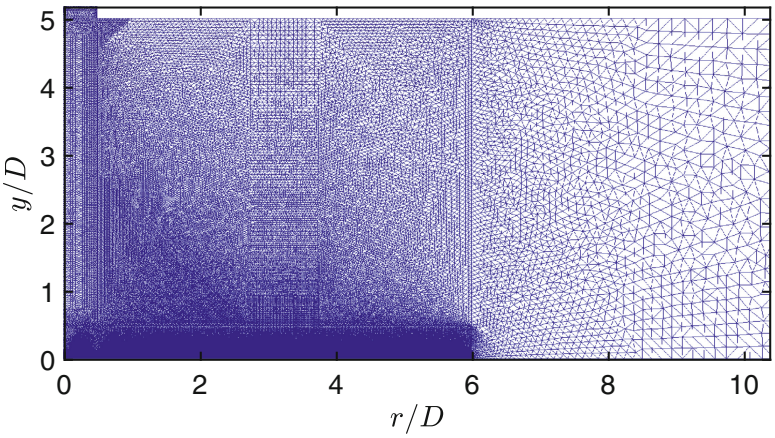

Fig. 2. Triangle mesh used for the stability analysis calculations. It consists of approximately 400,000 triangles.

4 DNS and DMD Results

In this section results from a DNS and DMD analysis of the impinging jet at $M = 0.8$ and $Re = 3300$ are presented.

As reported in detail by Wilke and Sesterhenn [14], it is observed that the vortex dynamics in an impinging jet system strongly affects the heat transfer at the impingement plate. In particular, primary vortices are induced within the shear layer of the free jet by Kelvin-Helmholtz instabilities and transported downstream until deflected because of the high pressure around the stagnation point, in the proximity of which they impinge the wall (see Fig. 3). Due to wall friction, counter-rotating secondary vortices are created in the impingement region, where their coupling with the primary ones results in a local enhancement of the heat flux through the plate.

Figure 4a shows the mean profile of the Nusselt number at the impingement plate, defined as

$$Nu = \frac{D}{\lambda \Delta T}\,\dot{q} \tag{21}$$

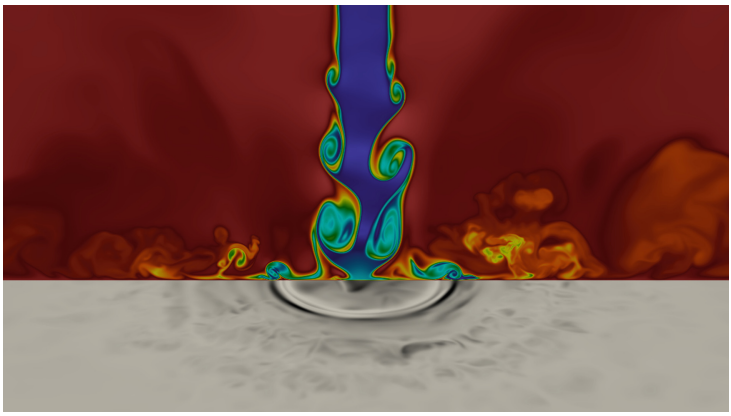

Fig. 3. Instantaneous temperature contours (blue: low temperature, red: high temperature) on a xy-plane passing through the jet axis, highlighting primary and secondary vorticity. In the bottom, contours of the Nusselt number at the target plate (black: high heat transfer, white: no heat transfer).

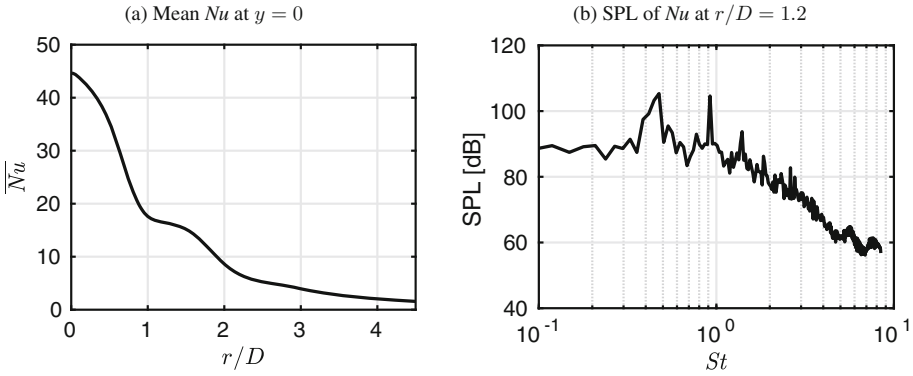

Fig. 4. Mean Nusselt number at the impingement plate (a) and average of the sound pressure levels of its instantaneous signal recorded at $r/D = 1.2$ (b).

with $\dot{q}$ the local heat flux at the wall, D the jet diameter, λ the thermal conductivity of the gas and $\Delta T = 80\,\mathrm{K}$ the difference between the temperature of the isothermal walls and the total temperature of the jet at the inlet. The mean Nusselt number exhibits its global maximum in the proximity of the jet axis, whereas a characteristic inflection point can be observed at $r/D \simeq 1.2$, with r/D the non-dimensional distance from the jet axis, in the region where primary and secondary vortices couple with the mechanism mentioned above.

In order to get insights into the characteristic frequencies of the system, a Fourier transform of the instantaneous Nu at $r/D = 1.2$ has been computed and averaged in the azimuthal direction. By observing Fig. 4b, two clear peaks can

be recognized at $St = 0.46$ and $St = 0.92$, with

$$St = \frac{Df}{U_\infty} \tag{22}$$

the Strouhal number and f the frequency.

By computing the dynamic modes of the system, the DMD enables to decompose a time-series of instantaneous flow field data into frequency components, supposing the existence of a linear operator that maps one snapshot of data with the next one. When the effects of non-linearity are not significant, the results of a DMD have shown to be comparable with those of a linear stability analysis of the same system. Here, we carried out a three-dimensional DMD using 120 snapshots taken every 510 time steps. This results in a sampling frequency corresponding to a St of about 9.2. Because of the significant amount of main memory required by the DMD algorithm, the snapshot matrix was build by taking, in each direction, every fourth data point from the full computing grid. Two dominant DMD modes have been found with associated Strouhal numbers corresponding to the frequency peaks of the Nusselt number signal at $r/D = 1.2$, i.e. $St = \pm 0.46$ and $St = \pm 0.92$, the second one being an harmonic of the first one (the dominant frequency).

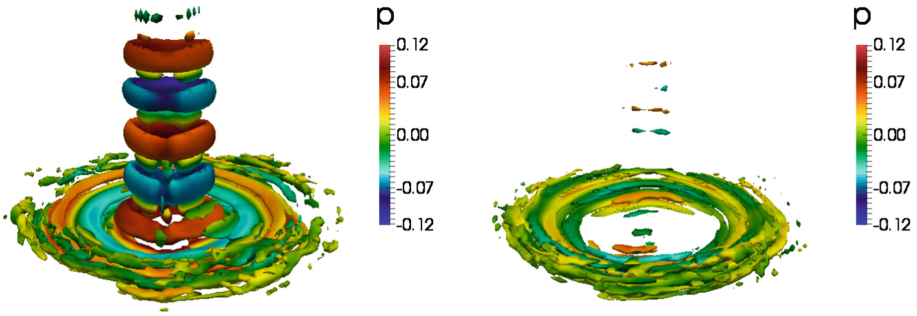

(a) $St = 0.46$ (b) $St = 0.92$

Fig. 5. Q contours of the dominant dynamic mode shapes ($Q = \pm 0.8\, U_\infty^2 D$) colored with the mode shapes of the non-dimensional pressure (normalized with p_∞).

Figure 5 shows the Q-component of the dominant DMD modes, being Q the second invariant of the velocity gradient tensor. Q is related to the flow vorticity and often employed in vortex identification techniques [23]. The structure of such modes is axisymmetric and appears related to toroidal vortexes. In particular, the DMD mode oscillating at $St = 0.46$ displays large structures related with the primary vorticity generated in the shear layer of the free jet region. On the contrary, the second DMD mode with $St = 0.92$ represents the harmonic of the dominant mode and, as expected, exhibits small spatial structures, which primarily appear in the wall jet region and are hence related to the secondary

vorticity. In conclusion, DMD results clearly show the existence of a dominant frequency (possibly with its harmonics) related to an axisymmetric self-sustained oscillation.

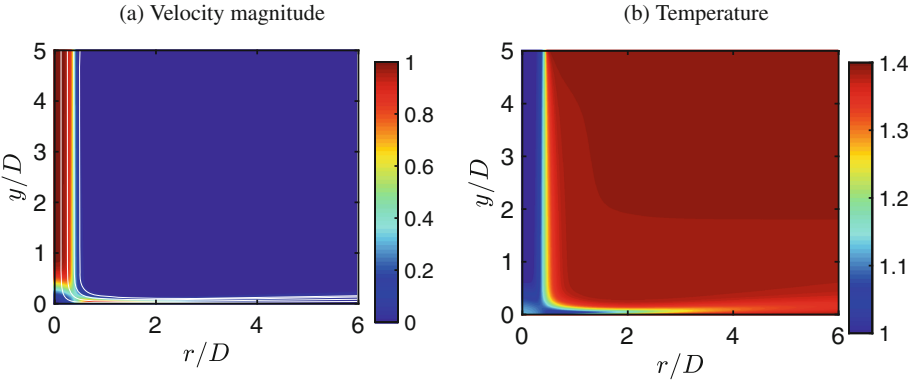

Fig. 6. Contours and streamlines of the steady-state base flow at $M = 0.8$ and $Re = 3000$.

5 Stability Analysis

In the following, results of the stability analysis of the impinging jet system are discussed. The analysis has been performed for Reynolds numbers ranging from 1800 to 3000 and Mach numbers ranging from 0 to 0.8.

Figure 6 shows the velocity and temperature components of the base flow. In the free jet region, the velocity in the jet core is essentially constant and orthogonal to the impingement plate. In proximity of the intersection between the jet axis and the wall, the jet is deviated radially because of the high pressure of the stagnation point. Further downstream, the flow develops a slowly growing boundary layer, until leaving the domain. The jet temperature appears constant in the core of the free jet region, undergoes a small increment in the stagnation region and nears the ambient temperature as the stream moves radially approaching the outlet.

As regards the stability analysis, we commence by considering the sprectrum of the eigenvalues solution of the problem in Eqs. (8a–d) for $Re = 2000$ and $M = 0.8$ (Fig. 7a). The said spectrum features a nearly unstable eigenvalue and the flow is therefore in these conditions nearly supercritical. The unstable eigenvalue is fairly isolated from the others and exhibits a pulsatance $\omega \simeq 2.8$, which corresponds to $St \simeq 0.455$. With increasing Reynolds number ($Re = 2500$) a second unstable mode with a slightly lower frequency appears. Notwithstanding, the first mode emerged remains dominant and practically retains its frequency. At $Re = 3000$, five unstable modes exists, with the previously dominant mode

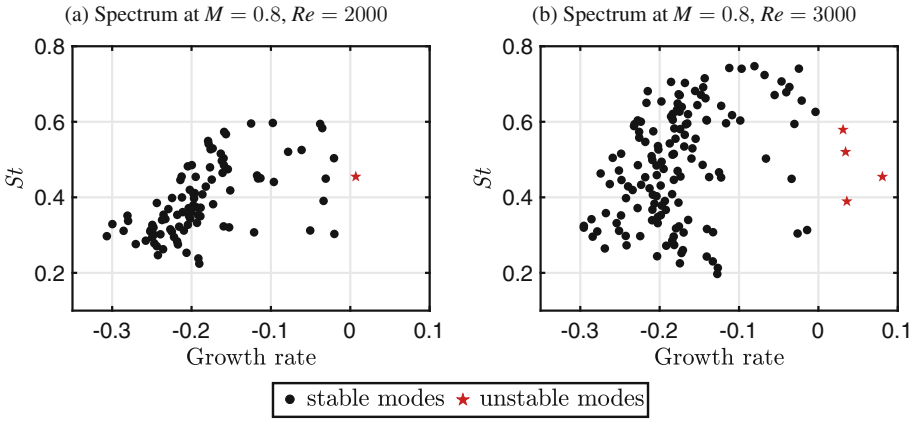

Fig. 7. Spectra of the eigenvalues solution of Eqs. (8a–d). The Strouhal number is given by $St = \omega/(2\pi)$, where ω is the eigenfrequency (pulsatance).

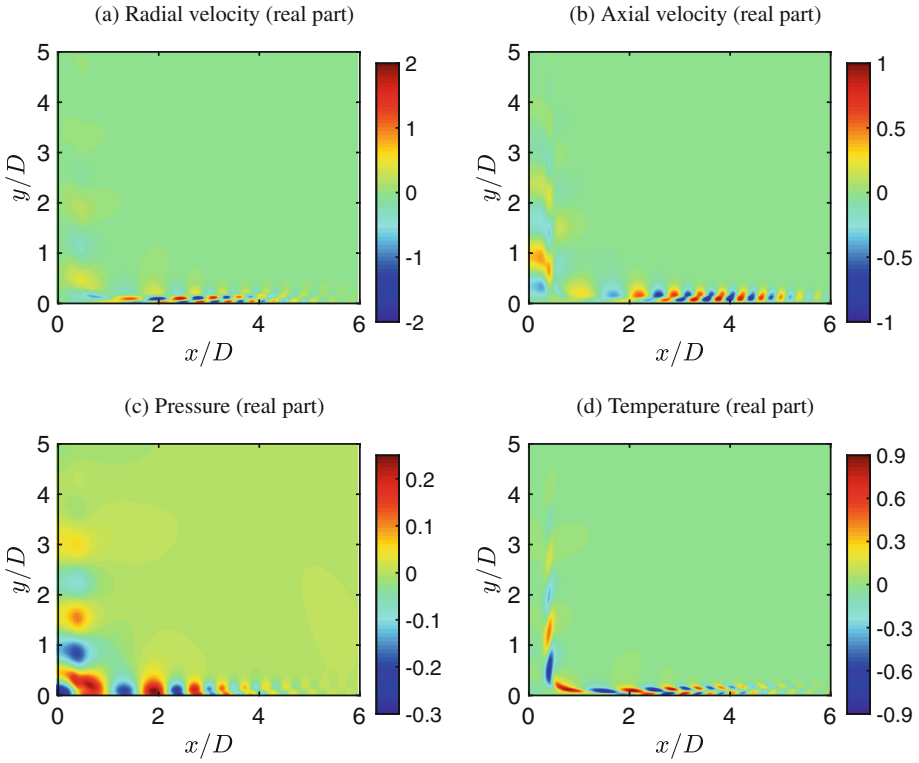

Fig. 8. Spatial structure of the dominant mode at $M = 0.8$ and $Re = 3000$ represented with the contours of the real parts of its components normalized with the maximum of the axial velocity absolute value.

maintaining the highest positive growth rate (Fig. 7b). It can be noted that its *St* number matches closely that of the first dominant mode found in the DMD analysis. In particular, the difference between the frequencies in terms of relative error is only of about 1%.

Figure 8 shows the spatial structure of the dominant mode at $Re = 3000$ and $M = 0.8$. All the components of mode feature strong fluctuations near the lowermost wall and, with the exception of the pressure, exhibit a similar structure. The pressure fluctuations reach indeed their highest strength in the proximity of the stagnation point.

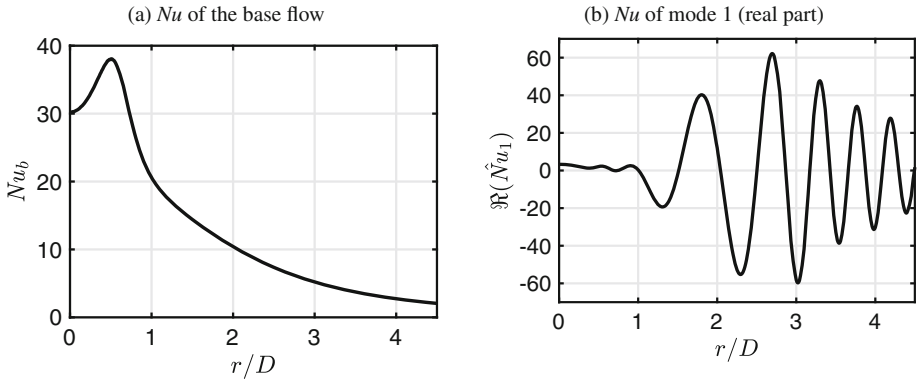

Fig. 9. Nusselt number at the impingement plate computed with the base flow (a) and the dominant mode (b) at $M = 0.8$ and $Re = 3000$.

Figure 9 shows the distribution of Nusselt number at the impingement plate for both the stationary base flow and the dominant mode. By comparing this figure with Fig. 4a it is possible to appreciate the role of the unsteadiness in the heat transfer process. Unsteady fluctuations (both related to the unstable periodic limit cycle related to the dominant unstable mode and to secondary instabilities and turbulent fluctuations) increase the heat-transfer efficiency reshaping the Nusselt distribution at the wall, especially in the impingement region, where the nonlinear interactions of the mode produce an important mean flow correction.

Let's now analyze the effect of the Reynolds and Mach numbers on the leading eigenmode. A parametric study has been performed and the resulting curves are reported in Fig. 10. On the left side we can see the growth rate, whereas on the left side the Strouhal numbers are shown. We note that the growth rate tends to increase with M for every Reynolds number, indicating that compressibility has a destabilizing effect on the impinging jet system. On the contrary, the Strouhal number generally decreases with increasing Mach number. Moreover, the curves in Fig. 10b collapses into one curve for $M \gtrsim 0.5$. This shows that the dominant frequency becomes independent of the Reynolds number in the high subsonic regime, although it does not considerably change even at lower Mach numbers.

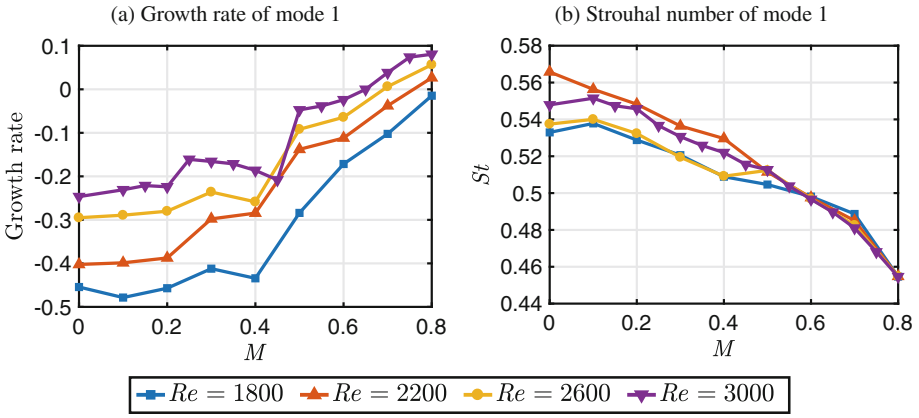

Fig. 10. Growth rate and Strouhal number of the mode 1 (i.e. the most unstable mode at $M = 0.8$ and $Re = 3000$) as a function of the Mach number plotted at different Reynolds numbers.

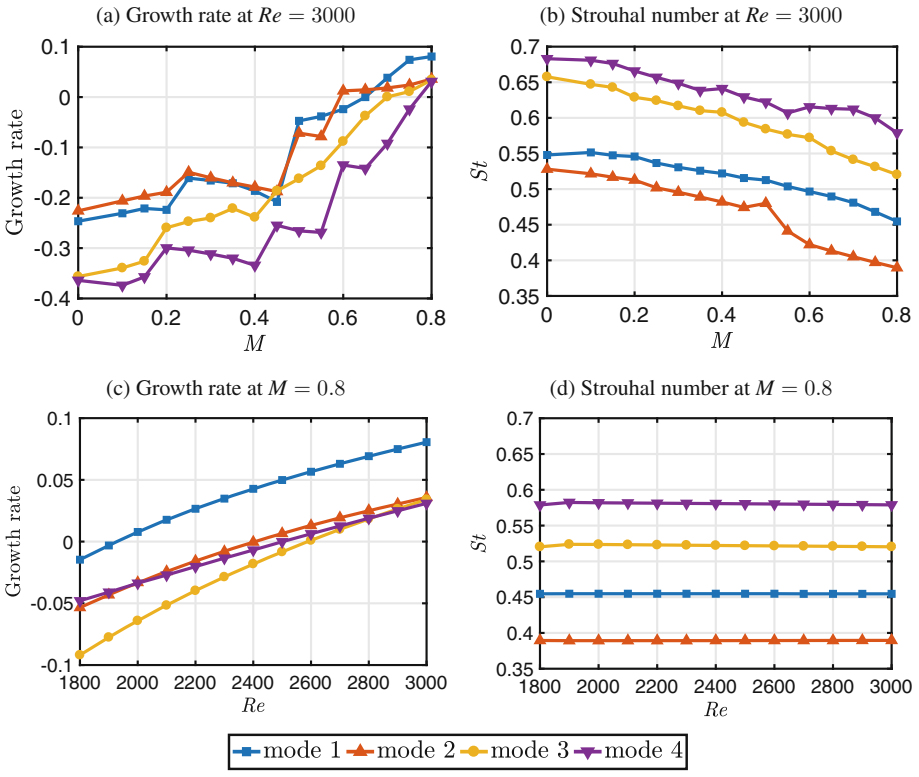

Fig. 11. Growth rate and Strouhal number of the dominant modes as a function of the Mach number at fixed $Re = 3000$ (a, b) and of the Reynolds number at fixed $M = 0.8$ (c, d).

With the help of Fig. 11 we move on to analyzing the change of growth rates and frequencies of the four leading modes with M at fixed $Re = 3000$ and with Re at fixed $M = 0.8$. It can be observed that the growth rate at fixed Reynolds number shows maxima and minima at different Mach numbers (Fig. 11a). Differently, the Strouhal number trend appears more regular with variations in M. As shown in Fig. 11c, we found that the critical Reynolds Re_c at $M = 0.8$ is approximately 1930. By looking at the Strouhal number change with Reynolds for $M = 0.8$ (Fig. 11d), we observe that, as already found for the most unstable mode, the frequencies of the leading modes are practically constant with varying Re. Furthermore, the frequencies appear to be quantized with a $\Delta St \simeq 0.065$, which can be conveniently seen with the help of Table 1 for the case with $M = 0.8$ and $Re = 3000$.

Table 1. Strouhal numbers of the unstable modes at $M = 0.8$ and $Re = 3000$.

	Mode 1	Mode 2	Mode 3	Mode 4
St	0.455	0.390	0.520	0.579

6 Conclusions

We performed a dynamic mode decomposition and a global stability analysis of compressible impinging jets in order to characterize the modal structure of the flow. Data for the DMD analysis were calculated by means of direct numerical simulation of the Navier-Stokes equations, carried out with at a Mach number of 0.8 and at a Reynolds number of about 3000. With respect to the global stability analysis, we considered a range of Mach and Reynolds numbers spanning from 0 to 0.8 and from 1800 to 3000, respectively. It has been found that at $M = 0.8$ the flow becomes globally unstable when $Re \simeq 2000$ and, in general, compressibility has a destabilizing effect.

The DMD analysis showed two dominant modes, with Strouhal numbers of 0.46 and 0.92, exist and that they are respectively linked with the primary and secondary vorticity in the flow. The interaction between primary and secondary vortices has been in fact proven crucial for the understanding of the physics of the heat transfer at the impingement plate [14]. This finding is also supported by the fact that the Fourier transform of the instantaneous heat flux in the region where primary and secondary vortices couple exhibits the same peak frequencies of the dominant DMD modes. Moreover, the frequency of the dominant DMD mode ($St = 0.46$) matches closely the eigenfrequency of the dominant mode obtained in the stability analysis ($St = 0.455$). In particular, their relative difference is only of about 1%.

Thanks to the stability analysis, a quantization of the frequencies associated with the dominant modes has been interestingly observed. This feature suggests

that the mechanism underlying the self-sustaining mode responsible for the generation of toroidal vortices (and often at the basis of strong tonal emissions) is caused by an acoustic resonance mechanism, as proposed by Towne et al. [24] and detected in other configurations (see for example, Yamouni et al. [10]). As a successive step of this work, a local stability analysis aimed at determining the existence of retrograde acoustic modes within the jet and their interaction with the Kelvin-Helmholtz instabilities could provide an qualitative-quantitative description of the mechanism underlying the self-sustaining instability described above and return important information for the design of effective and efficient control algorithms.

Acknowledgements. The authors gratefully acknowledge support by the Deutsche Forschungsgemeinschaft (DFG) as part of collaborative research center SFB 1029 "Substantial efficiency increase in gas turbines through direct use of coupled unsteady combustion and flow dynamics" on project B04.

References

1. Martin, H.: Heat and mass transfer between impinging gas jets and solid surfaces. Adv. Heat Transfer **13**, 1–60 (1977)
2. Janetzke, T.: Experimentelle Untersuchungen zur Effizienzsteigerung von Prallkühlkonfigurationen durch dynamische Ringwirbelhoher amplitude (Experimental investigations on efficiency enhancement of impingement cooling configurations by means of high-amplitude dynamical ring vortices). Ph.D. thesis, Technische Universität Berlin, Mensch und Buch Verlag, Berlin (2010)
3. Camarri, S.: Flow control design inspired by linear stability analysis. Acta Mech. **226**(4), 979–1010 (2015)
4. Citro, V., Tchoufag, J., Fabre, D., Giannetti, F., Luchini, P.: Linear stability and weakly nonlinear analysis of the flow past rotating spheres. J. Fluid Mech. **807**, 62–86 (2016)
5. Citro, V., Giannetti, F., Pralits, J.: Three-dimensional stability, receptivity and sensitivity of non-newtonian flows inside open cavities. Fluid Dyn. Res. **47**(1), 1–14 (2015)
6. Citro, V., Siconolfi, L., Fabre, D., Giannetti, F., Luchini, P.: Stability and sensitivity analysis of the secondary instability in the sphere wake. AIAA J. **55**(11), 3661–3668 (2017)
7. Giannetti, F., Camarri, S., Citro, V.: Sensitivity analysis and passive control of the secondary instability in the wake of a cylinder. J. Fluid Mech. **864**, 45–72 (2019)
8. Siconolfi, L., Citro, V., Giannetti, F., Camarri, S., Luchini, P.: Towards a quantitative comparison between global and local stability analysis. J. Fluid Mech. **819**, 147–164 (2017)
9. Meliga, P., Chomaz, J.M.: Global modes in a confined impinging jet: application to heat transfer and control. Theoret. Comput. Fluid Dyn. **25**(1–4), 179–193 (2011)
10. Yamouni, S., Sipp, D., Jacquin, L.: Interaction between feedback aeroacoustic and acoustic resonance mechanisms in a cavity flow: a global stability analysis. J. Fluid Mech. **717**, 134–165 (2013)
11. Fani, A., Citro, V., Giannetti, F., Auteri, F.: Computation of the bluff-body sound generation by a self-consistent mean flow formulation. Phys. Fluids **30**(3), 036102 (2018)

12. Fabre, D., Citro, V., Sabino, D., Bonnefis, P., Sierra, J., Giannetti, F., Pigou, M.: A practical review on linear and nonlinear global approaches to flow instabilities. Appl. Mech. Rev. **70**(6), 060802 (2018)
13. Schmid, P.J., Sesterhenn, J.: Dynamic mode decomposition of numerical and experimental data. In: Bulletin of the American Physical Society, 61st Annual Meeting of the APS Division of Fluid Dynamics, p. 208. American Physical Society, San Antonio (2008)
14. Wilke, R., Sesterhenn, J.: Numerical simulation of subsonic and supersonic impinging jets II. In: Nagel, W.E., Kröner, D.H., Resch, M.M. (eds.) High Performance Computing in Science and Engineering 2016, pp. 425–441. Springer, Cham (2016)
15. Wilke, R., Sesterhenn, J.: Statistics of fully turbulent impinging jets. J. Fluid Mech. **825**, 795–824 (2017)
16. Drazin, P.G., Reid, W.H.: Hydrodynamic Stability. Cambridge University Press, Cambridge (2004)
17. Schmid, P.J.: Dynamic mode decomposition of numerical and experimental data. J. Fluid Mech. **656**, 5–28 (2010)
18. Sesterhenn, J.: A characteristic-type formulation of the Navier-Stokes equations for high order upwind schemes. Comput. Fluids **30**(1), 37–67 (2000)
19. Lele, S.K.: Compact finite difference schemes with spectral-like resolution. J. Comput. Phys. **103**(1), 16–42 (1992)
20. Adams, N., Shariff, K.: A high-resolution hybrid compact-ENO scheme for shock-turbulence interaction problems. J. Comput. Phys. **127**(1), 27–51 (1996)
21. Amestoy, P.R., Duff, I.S., L'Excellent, J.Y., Koster, J.: A fully asynchronous multifrontal solver using distributed dynamic scheduling. SIAM J. Matrix Anal. Appl. **23**(1), 15–41 (2001)
22. Rowley, C.W., Colonius, T., Basu, A.J.: On self-sustained oscillations in two-dimensional compressible flow over rectangular cavities. J. Fluid Mech. **455**, 315–346 (2002)
23. da Silva, C.B., Pereira, J.C.: Invariants of the velocity-gradient, rate-of-strain, and rate-of-rotation tensors across the turbulent/nonturbulent interface in jets. Phys. Fluids **20**(5), 055101 (2008)
24. Towne, A., Cavalieri, A.V., Jordan, P., Colonius, T., Schmidt, O., Jaunet, V., Brès, G.A.: Acoustic resonance in the potential core of subsonic jets. J. Fluid Mech. **825**, 1113–1152 (2017)